

## Theory of deterministic down-conversion of single photons occurring at an impedance-matched $\Lambda$ system

Kazuki Koshino<sup>1,5</sup>, Kunihiro Inomata<sup>2</sup>, Tsuyoshi Yamamoto<sup>2,3</sup>  
and Yasunobu Nakamura<sup>2,4</sup>

<sup>1</sup> College of Liberal Arts and Sciences, Tokyo Medical and Dental University,  
2-8-30 Konodai, Ichikawa 272-0827, Japan

<sup>2</sup> RIKEN Center for Emergent Matter Science, Wako, Saitama 351-0198, Japan

<sup>3</sup> NEC Smart Energy Research Laboratories, Tsukuba, Ibaraki 305-8501, Japan

<sup>4</sup> Research Center for Advanced Science and Technology, University of Tokyo,  
Meguro-ku, Tokyo 153-8904, Japan

E-mail: [kazuki.koshino@osamember.org](mailto:kazuki.koshino@osamember.org)

*New Journal of Physics* **15** (2013) 115010 (15pp)

Received 31 July 2013

Published 15 November 2013

Online at <http://www.njp.org/>

doi:10.1088/1367-2630/15/11/115010

**Abstract.** We theoretically investigate the optical response of a  $\Lambda$  system interacting with a semi-infinite waveguide field. In particular, we focus on the case of an impedance-matched  $\Lambda$  system, in which the two decay rates from the top level are identical. We derive the analytical formulae to evaluate the amplitude and the power spectrum of the output field, and present numerical results assuming an implementation by a circuit quantum electrodynamics system. For a low input power (single-photon regime), input photons are down-converted deterministically by inducing the Raman transition in the  $\Lambda$  system. In contrast, for a high input power (multi-photon regime), the conversion efficiency decreases because of the saturation of the  $\Lambda$  system.

<sup>5</sup> Author to whom any correspondence should be addressed.



Content from this work may be used under the terms of the [Creative Commons Attribution 3.0 licence](http://creativecommons.org/licenses/by/3.0/). Any further distribution of this work must maintain attribution to the author(s) and the title of the work, journal citation and DOI.

**Contents**

<b>1. Introduction</b>	<b>2</b>
<b>2. Formulation</b>	<b>3</b>
2.1. Hamiltonian . . . . .	3
2.2. State vector . . . . .	5
2.3. Heisenberg equations . . . . .	5
2.4. Amplitude . . . . .	5
2.5. Power spectrum . . . . .	6
<b>3. Numerical results</b>	<b>6</b>
3.1. Amplitude: monochromatic input . . . . .	7
3.2. Amplitude: dichromatic input . . . . .	8
3.3. Power spectrum . . . . .	9
<b>4. Summary</b>	<b>11</b>
<b>Acknowledgments</b>	<b>11</b>
<b>Appendix A. Implementation in circuit quantum electrodynamics</b>	<b>12</b>
<b>Appendix B. Calculation of <math>S_i(\omega)</math></b>	<b>13</b>
<b>References</b>	<b>14</b>

**1. Introduction**

One of the hottest research topics in recent quantum optics is waveguide quantum electrodynamics (QED), in which radiation from a single emitter (atom, quantum dot, superconducting qubit, etc) is guided completely to a one-dimensional field propagating in a waveguide [1]. Such one-dimensional optical setups have been usually realized by coupling an emitter to a resonator and then to a propagating field, enhancing the one dimensionality by the Purcell effect [2–6]. However, in circuit QED systems [7–18], where superconducting qubits strongly interact with the microwave fields propagating in waveguides, we can achieve excellent one dimensionality by simply coupling a qubit directly to an open waveguide field. In these waveguide-based quantum optics systems, radiation from an emitter inevitably interferes with the excitation field applied via the waveguide due to its one dimensionality. This results in a drastic enhancement of the cross section in the light–matter interaction. By using a single two-level emitter, the following phenomena that are characteristic of one-dimensional systems have been achieved: the giant optical nonlinearity sensitive to single photons [2, 5, 7] and the perfect reflection of single photons [6, 8–10]. Further developments have been accomplished by using the second excited state of the qubit, i.e. the ladder-type three-level system [11–14]. These results imply that input photons deterministically interact with an emitter, and open the possibilities of deterministic quantum control by single photons. Direct coupling of an emitter to a tapered fiber or a plasmonic nanowire is also promising for implementation of one-dimensional quantum-optics systems [19, 20]. We can also expect one-dimensional effects in free space by using focused light beams [21, 22].

By using a  $\Lambda$ -type three-level system as an emitter in waveguide QED, we can enhance the probability that the input photon induces the Raman transition and accordingly switches the quantum state of the  $\Lambda$  system. In particular, it has been theoretically revealed that this

probability may reach unity when the following conditions are satisfied: (i) the  $\Lambda$  system is coupled to the waveguide field in reflection geometry; and (ii) the two radiative decay rates from the top level of the  $\Lambda$  system are identical [23–28]. Then, the input photons are never reflected coherently and the amplitude of the reflected wave vanishes accordingly. We refer to this phenomenon as the impedance matching by a  $\Lambda$  system, in analogy with properly terminated electric circuits. Such impedance-matched  $\Lambda$  systems are attractive for quantum information processing, since the expected deterministic quantum dynamics is applicable to quantum memories [24–26], single-photon transistors [27, 28], photon sorters [29], photon–photon gates [24–26, 30, 31] and single-photon detectors in microwave domain [32–34].

Recently, we showed that an impedance-matched  $\Lambda$  system can be implemented by a practical circuit QED system in the dispersive-coupling regime [35, 36]. In this work, assuming this circuit QED implementation, we theoretically investigate the optical response of an impedance-matched  $\Lambda$  system. We consider a classical continuous microwave as the input, and analyze the coherent amplitude and the power spectrum of the output field. However, the essence of the results remains unchanged when we use single photons as the input, as long as the bandwidths of the input photons are sufficiently narrow. We will show that, for a low input power, all of the input photons are down-converted upon a single interaction with the  $\Lambda$  system as a result of a deterministic Raman transition [23]. This is reflected in spectroscopy as the complete extinction of the coherent amplitude and the appearance of a dominant peak at the down-converted frequency in the power spectrum. For a higher input power, we observe nonlinear optical effects such as power broadening in the spectra and the degradation of the down-conversion efficiency.

The remainder of this paper is organized as follows. We present the theoretical model and derive analytical formulae to calculate the amplitude and power spectrum of the output field in section 2. By assuming a circuit QED implementation, we discuss the numerical results in section 3. Section 4 summarizes this study. We discuss implementation of an impedance-matched  $\Lambda$  system by a circuit QED system in appendix A, and present the technical details of the calculation of the power spectrum in appendix B.

## 2. Formulation

### 2.1. Hamiltonian

In this study, we analyze the optical response of a three-level  $\Lambda$  system to a one-dimensional photon field propagating in a semi-infinite waveguide (figure 1). We denote the three levels and their frequencies with  $|n\rangle$  and  $\omega_n$  ( $n = 1, 2, 3$ ) from the lowest. Putting  $\hbar = v = 1$ , where  $v$  is the microwave velocity in the waveguide, the Hamiltonian of the overall system is

$$\mathcal{H} = \mathcal{H}_s + \mathcal{H}_{\text{sw}} + \mathcal{H}_{\text{se}}, \quad (1)$$

$$\mathcal{H}_s = \sum_m \omega_m \sigma_{mm}, \quad (2)$$

$$\mathcal{H}_{\text{sw}} = \int dk k a_k^\dagger a_k + \sum_{m,n} \int dk \sqrt{\frac{\kappa_{mn}}{2\pi}} \left( \sigma_{mn} a_k + a_k^\dagger \sigma_{nm} \right), \quad (3)$$

$$\mathcal{H}_{\text{se}} = \int dk k b_k^\dagger b_k + \sum_{m,n} \int dk \sqrt{\frac{\gamma_{mn}}{2\pi}} \left( \sigma_{mn} b_k + b_k^\dagger \sigma_{nm} \right), \quad (4)$$

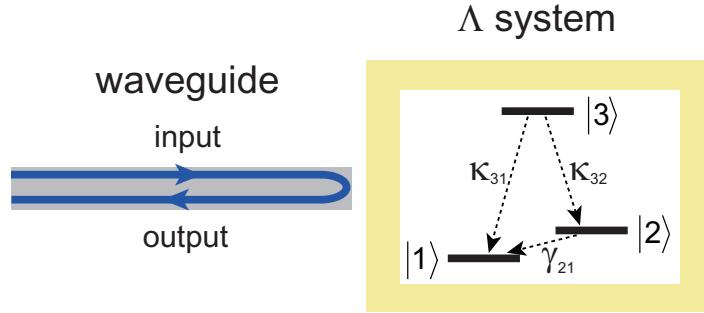


**Figure 1.** Schematic representation of the setup. A three-level  $\Lambda$  system interacts with the waveguide photons in reflection geometry.  $\omega_n$  is the eigenfrequency of level  $|n\rangle$ , and  $\kappa_{mn}$  ( $\gamma_{mn}$ ) is the decay rate into the waveguide (environment). Assuming a circuit QED implementation, we employ the following parameters in numerical simulations:  $(\omega_1, \omega_2, \omega_3)/2\pi = (0, 0.08, 10.02)$  GHz and  $(\kappa_{31}, \kappa_{32}, \gamma_{21})/2\pi = (10, 10, 1)$  MHz. Other decay rates are set to zero.

where  $\sigma_{mn} = |m\rangle\langle n|$ , and  $a_k$  is the annihilation operator of a waveguide photon with wavenumber  $k$ . The environment is modeled by a one-dimensional boson field and  $b_k$  denotes its annihilation operator.  $\kappa_{mn}$  is the decay rate for  $|m\rangle \rightarrow |n\rangle$  transition emitting a waveguide photon.  $\gamma_{mn}$  is the decay rate for  $|m\rangle \rightarrow |n\rangle$  transition dissipating the energy into the environment. We assumed that the microwave velocity and the coupling constants ( $\kappa_{mn}$  and  $\gamma_{mn}$ ) are constant in the frequency range of interest.

Throughout this study, we consider the case in which the present setup is highly one-dimensional ( $\kappa_{mn} \gg \gamma_{mn}$ ) and satisfies the impedance-matching condition ( $\kappa_{31} = \kappa_{32}$ ). This case is of particular interest, because the Raman transition ( $|1\rangle \rightarrow |3\rangle \rightarrow |2\rangle$ ) is induced deterministically by a single input photon, due to destructive interference between the incident and elastically scattered photons. These conditions can be satisfied in a driven circuit QED system under a proper choice of the drive frequency and the power (see appendix A).

For later convenience, we define the real-space representation  $\tilde{a}_r$  of the waveguide field. We may simply define it as the Fourier transform of  $a_k$ :

$$\tilde{a}_r = (2\pi)^{-1/2} \int dk e^{ikr} a_k \quad (5)$$

neglecting the phase factor upon reflection [37, 38]. In this representation, the field interacts with the  $\Lambda$  system at  $r = 0$ , and the  $r < 0$  ( $r > 0$ ) region represents the incoming (outgoing) field. Throughout this study, we work in the Heisenberg picture and denote the operator  $A$  at time  $t$  with  $A(t) [= e^{i\mathcal{H}t} A e^{-i\mathcal{H}t}]$ . The conventional input and output field operators of the waveguide field are, respectively, defined by

$$a_{\text{in}}(t) = \tilde{a}_{-0}(t), \quad (6)$$

$$a_{\text{out}}(t) = \tilde{a}_{+0}(t). \quad (7)$$

$b_{\text{in}}(t)$  and  $b_{\text{out}}(t)$  are defined similarly.

## 2.2. State vector

In this study, we apply a continuous probe field  $E_{\text{in}}(r, t)$  via the waveguide and measure the reflected field in the stationary state. We assume that the  $\Lambda$  system is in its ground state  $|1\rangle$  initially ( $t = 0$ ). Then, the initial state vector of the whole system is given by

$$|\Psi_i\rangle = \mathcal{N} \exp\left(\int dr E_{\text{in}}(r, 0) \tilde{a}_r^\dagger\right) |1\rangle, \quad (8)$$

where  $\mathcal{N}$  is a normalization constant. In this study, we consider up to two tones  $\mu_1$  and  $\mu_2$  (close to  $\omega_{31}$  and  $\omega_{32}$ , respectively, where  $\omega_{ij} = \omega_i - \omega_j$ ) in the input wave. Therefore,

$$E_{\text{in}}(r, t) = E_1 e^{i\mu_1(r-t)} + E_2 e^{i\mu_2(r-t)}. \quad (9)$$

## 2.3. Heisenberg equations

From the Hamiltonian of equation (1), we can rigorously derive the following operator equations. The relation between the incoming ( $r < 0$ ) and outgoing ( $r > 0$ ) waveguide fields is  $\tilde{a}_r(t) = \tilde{a}_{r-t}(0) - i\theta(r)\theta(t-r) \sum_{m,n} \sqrt{\kappa_{mn}} \sigma_{nm}(t-r)$ , where  $\theta(r)$  is the Heaviside step function. By using the input and output field operators defined by equations (6) and (7), we obtain the input–output relation of the conventional form [39]

$$a_{\text{out}}(t) = a_{\text{in}}(t) - i \sum_{m,n} \sqrt{\kappa_{mn}} \sigma_{nm}(t). \quad (10)$$

The input–output relation for  $b_{\text{in}}(t)$  and  $b_{\text{out}}(t)$  is obtained by replacing  $\kappa$  with  $\gamma$ .

The Heisenberg equation for the system operator  $\sigma_{ij}$  is given by

$$\frac{d}{dt} \sigma_{ij} = \sum_{m,n} \left[ \eta_{ijmn}^{(1)} \sigma_{mn} - i\eta_{ijmn}^{(2)} \sigma_{mn} a_{\text{in}}(t) - i\eta'_{ijmn}{}^{(2)} \sigma_{mn} b_{\text{in}}(t) + i\eta_{jinm}^{(2)} a_{\text{in}}^\dagger(t) \sigma_{mn} + i\eta_{jinm}^{(2)} b_{\text{in}}^\dagger(t) \sigma_{mn} \right], \quad (11)$$

where  $\eta_{ijmn}^{(1)} = i(\omega_i - \omega_j) \delta_{im} \delta_{jn} + \xi_{ijmn}^{(1)} + \xi'_{ijmn}{}^{(1)}$ ,  $\eta_{ijmn}^{(2)} = \delta_{im} \sqrt{\kappa_{jn}} - \delta_{jn} \sqrt{\kappa_{mi}}$  and  $\xi_{ijmn}^{(1)} = \sqrt{\kappa_{mi} \kappa_{nj}} - \delta_{im} \sum_{\nu} \sqrt{\kappa_{j\nu} \kappa_{n\nu}}/2 - \delta_{jn} \sum_{\nu} \sqrt{\kappa_{i\nu} \kappa_{m\nu}}/2$ .  $\xi'_{ijmn}{}^{(1)}$  and  $\eta'_{ijmn}{}^{(2)}$  are obtained by replacing  $\kappa$  with  $\gamma$ .

## 2.4. Amplitude

In order to calculate the amplitude of the reflected field, we need the one-point correlation functions of the system operator,  $\langle \sigma_{mn}(t) \rangle = \langle \Psi_i | \sigma_{mn}(t) | \Psi_i \rangle$ . When the input field contains up to two tones as in equation (9),  $\langle \sigma_{mn}(t) \rangle$  evolves in time as  $\langle \sigma_{mn}(t) \rangle = \sum_{p,q} s_{mn}^{p,q} e^{i(p\mu_1 + q\mu_2)t}$  in the stationary state, where  $p, q = 0, \pm 1, \dots$ . The simultaneous equations to determine  $s_{mn}^{p,q}$  are obtained from equation (11). Note that the input field operators  $a_{\text{in}}(t) [= \tilde{a}_{-t}(0)]$  and  $b_{\text{in}}(t) [= \tilde{b}_{-t}(0)]$  can be rigorously replaced with  $E_{\text{in}}(0, t)$  and 0, respectively, since the initial state vector  $|\Psi_i\rangle$  is an eigenstate of these operators. Thus, we have

$$i(p\mu_1 + q\mu_2) s_{ij}^{p,q} = \sum_{m,n} \left[ \eta_{ijmn}^{(1)} s_{mn}^{p,q} - iE_1 \eta_{ijmn}^{(2)} s_{mn}^{p+1,q} - iE_2 \eta_{ijmn}^{(2)} s_{mn}^{p,q+1} + iE_1^* \eta_{jinm}^{(2)} s_{mn}^{p-1,q} + iE_2^* \eta_{jinm}^{(2)} s_{mn}^{p,q-1} \right]. \quad (12)$$

The diagonal components of these equations are not linearly independent since  $\sum_m \sigma_{mm} = \hat{1}$ . Therefore, we should replace one of them with the following equality:

$$\sum_m s_{mm}^{p,q} = \delta_{p0} \delta_{q0}. \quad (13)$$

By solving these simultaneous equations numerically, we determine  $s_{mn}^{p,q}$ . These simultaneous equations have infinite dimension in principle, but reliable numerical results are obtained by setting  $p, q = 0, \dots, \pm 3$ .

The coherent amplitude of the reflected field is determined by  $E_{\text{out}}(r, t) = \langle \tilde{a}_r(t) \rangle$ . In particular, we evaluate the field at  $r = +0$ , i.e.  $E_{\text{out}}(0, t) = \langle a_{\text{out}}(t) \rangle$ . From the input–output relation of equation (10), we have

$$E_{\text{out}}(0, t) = E_{\text{in}}(0, t) - i \sum_{m,n} \sqrt{\kappa_{mn}} \langle \sigma_{nm}(t) \rangle. \quad (14)$$

In the stationary state,  $E_{\text{out}}(0, t)$  evolves as  $E_{\text{out}}(0, t) = \sum_{p,q} E_{\text{out}}^{p,q} e^{i(p\mu_1 + q\mu_2)t}$ . When we measure the reflection coefficient, the field components at the fundamental frequencies,  $\mu_1$  and  $\mu_2$ , are relevant. They are, respectively, given by  $E_{\text{out}}(\mu_1) = E_1 - i \sum_{m,n} \sqrt{\kappa_{mn}} s_{nm}^{-1,0}$  and  $E_{\text{out}}(\mu_2) = E_2 - i \sum_{m,n} \sqrt{\kappa_{mn}} s_{nm}^{0,-1}$ . The reflection coefficients are, respectively, given by  $r(\mu_1) = 1 - i \sum_{m,n} \sqrt{\kappa_{mn}} s_{nm}^{-1,0} / E_1$  and  $r(\mu_2) = 1 - i \sum_{m,n} \sqrt{\kappa_{mn}} s_{nm}^{0,-1} / E_2$ .

### 2.5. Power spectrum

The power spectrum density  $S(\omega)$  of the reflected field is calculated by  $S(\omega) = \text{Re} \int_0^\infty d\tau e^{i\omega\tau} \langle a_{\text{out}}^\dagger(t) a_{\text{out}}(t+\tau) \rangle / \pi$ . This consists of the coherent and incoherent components. The coherent component is determined by the amplitude of the reflected field. It is given by

$$S_c(\omega) = |E_{\text{out}}(\mu_1)|^2 \delta(\omega - \mu_1) + |E_{\text{out}}(\mu_2)|^2 \delta(\omega - \mu_2) + \dots \quad (15)$$

On the other hand, the incoherent component is determined by the two-point correlation functions of the system operators,  $\langle \sigma_{uv}(t), \sigma_{ij}(t+\tau) \rangle$ , where  $\langle A, B \rangle = \langle AB \rangle - \langle A \rangle \langle B \rangle$ . Similar to the one-point correlation function, this quantity is also written as  $\langle \sigma_{uv}(t), \sigma_{ij}(t+\tau) \rangle = \sum_{p,q} \langle \sigma_{uv}, \sigma_{ij}(\tau) \rangle^{p,q} e^{i(p\mu_1 + q\mu_2)t}$  in the stationary state, and the static component ( $p = q = 0$ ) is measured in actual experiments. The incoherent component is then given by

$$S_i(\omega) = \text{Re} \sum_{u,v,i,j} \sqrt{\kappa_{uv} \kappa_{ji}} \int_0^\infty d\tau e^{i\omega\tau} \langle \sigma_{uv}, \sigma_{ij}(\tau) \rangle^{0,0} / \pi. \quad (16)$$

We present the technical details of the numerical calculation of  $S_i(\omega)$  in appendix B.

## 3. Numerical results

In this section, we present the numerical results. Assuming implementation by a practical circuit QED system [35, 36], we employ the following parameters in numerical simulations (see appendix A for derivation):  $(\omega_1, \omega_2, \omega_3)/2\pi = (0, 0.08, 10.02)$  GHz and  $(\kappa_{31}, \kappa_{32}, \gamma_{21})/2\pi = (10, 10, 1)$  MHz. Other decay rates are assumed to be zero.

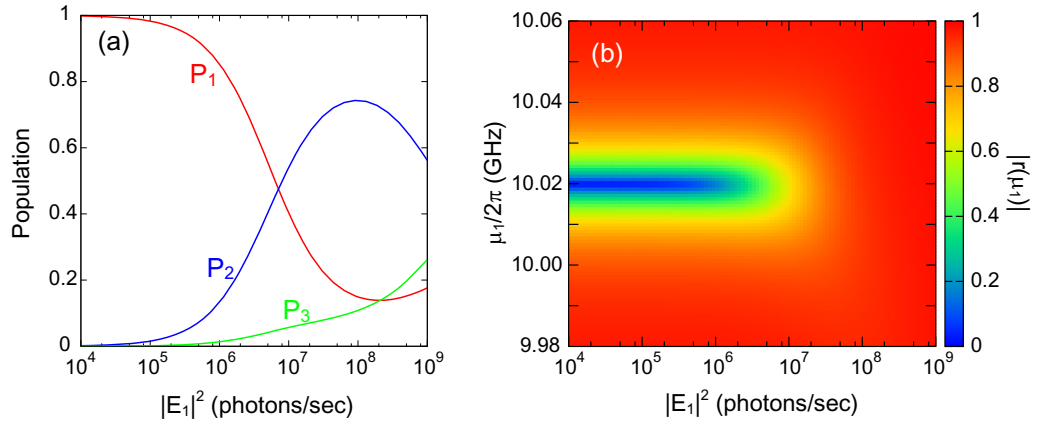


**Figure 2.** (a) Stationary populations of the three levels as functions of the input power  $|E_1|^2$ . The input frequency is fixed at  $\omega_{31}$ .  $|1\rangle$  is dominantly populated for  $|E_1|^2 \lesssim \gamma_{21}$  (single-photon regime), whereas  $|2\rangle$  becomes more populated for  $|E_1|^2 \gtrsim \gamma_{21}$  (multi-photon regime). (b) Reflection coefficient  $|r(\mu_1)|$  as a function of the input power  $|E_1|^2$  and frequency  $\mu_1$ . The reflection amplitude vanishes when the input field is resonant ( $\mu_1 = \omega_{31}$ ) and weak (single-photon regime).

### 3.1. Amplitude: monochromatic input

Here we assume a monochromatic input, i.e.  $E_{\text{in}}(0, -t) = E_1 e^{-i\mu_1 t}$ , and discuss the amplitude of the reflected field. The input frequency is tuned close to the  $|1\rangle \leftrightarrow |3\rangle$  transition ( $\mu_1 \simeq \omega_{31}$ ), where the input photons interact with the  $\Lambda$  system most efficiently. We quantify the input power by  $|E_1|^2$ , which has a dimension of inverse of time and represents the input photon number per unit time.

Since the present system is impedance-matched ( $\kappa_{31} = \kappa_{32}$ ), a resonant input photon induces the Raman transition  $|1\rangle \rightarrow |3\rangle \rightarrow |2\rangle$  almost deterministically and  $|2\rangle \rightarrow |1\rangle$  relaxation follows afterwards. The bottleneck process in this cycle is  $|2\rangle \rightarrow |1\rangle$  relaxation since  $\kappa_{31}, \kappa_{32} \gg \gamma_{21}$ . Therefore, the maximal rate of the down-conversion by this  $\Lambda$  system is  $\gamma_{21}$ . On the other hand, photons are input into the  $\Lambda$  system with a rate of  $|E_1|^2$ . Therefore, we can define the single-photon and multi-photon regimes by  $|E_1|^2 \lesssim \gamma_{21}$  and  $|E_1|^2 \gtrsim \gamma_{21}$ , respectively. In the single-photon regime, only a single photon is involved in the dynamics of the  $\Lambda$  system and the linear optical response is expected. In contrast, in the multi-photon regime, more than two photons are involved and nonlinear effects appear.

The stationary populations of the three levels,  $P_n = \langle \sigma_{nn} \rangle$ , are plotted as functions of the input power in figure 2(a), where  $\mu_1 = \omega_{31}$ . Since  $\gamma_{21}/2\pi = 1$  MHz, the boundary between the single-photon and multi-photon regimes is located at  $|E_1|^2 \sim 10^6 \text{ s}^{-1}$ . We observe that the ground level  $|1\rangle$  is populated dominantly in the single-photon regime. In contrast, in the multi-photon regime, the metastable level  $|2\rangle$  becomes more populated than  $|1\rangle$  because of the saturation.

The reflection coefficient is plotted as a function of the input power  $|E_1|^2$  and frequency  $\mu_1$  in figure 2(b). We observe a dip centered at  $\mu_1 = \omega_{31}$  in the single-photon regime. The width of the dip is determined by  $\kappa_{31}$  ( $2\pi \times 10$  MHz). In the single-photon regime, the reflection

coefficient is analytically given by

$$r(\mu_1) = |E_{\text{out}}/E_{\text{in}}| = \left| \frac{-\kappa_{31} + \kappa_{32} + \gamma_{31} + \gamma_{32} + i(\mu_1 - \omega_{31})}{\kappa_{31} + \kappa_{32} + \gamma_{31} + \gamma_{32} + i(\mu_1 - \omega_{31})} \right|. \quad (17)$$

Therefore, the conditions for the complete extinction of reflection (in other words, impedance matching) are  $\mu_1 = \omega_{31}$  and  $\kappa_{31} = \kappa_{32} + \gamma_{31} + \gamma_{32}$ . Note that, even under the existence of finite dissipation ( $\gamma_{31}$  and  $\gamma_{32}$ ), impedance matching may take place. The physical origin of this phenomenon is the destructive interference between the input field and elastically scattered field, which is characteristic of one-dimensional optical systems. For a higher input power in the multi-photon regime, level  $|2\rangle$  is more populated than  $|1\rangle$  because of the saturation (figure 2(a)). Then, the input field at  $\omega_{31}$  tends to be reflected without interacting with the  $\Lambda$  system, and the amplitude of the reflected field increases monotonically in the multi-photon regime.

### 3.2. Amplitude: dichromatic input

Here we assume a dichromatic input, i.e.  $E_{\text{in}}(0, -t) = E_1 e^{-i\mu_1 t} + E_2 e^{-i\mu_2 t}$ , where  $\mu_1 \simeq \omega_{31}$  and  $\mu_2 \simeq \omega_{32}$ . We refer to  $E_1 e^{-i\mu_1 t}$  ( $E_2 e^{-i\mu_2 t}$ ) as the first (second) field in this subsection. The stationary populations of the three levels are plotted as functions of  $|E_2|^2$  in figure 3(a), where  $\mu_1 = \omega_{31}$ ,  $\mu_2 = \omega_{32}$  and  $|E_1|^2 = 10^5 \text{ s}^{-1}$  (single-photon regime). We observe that, except for the cases where the second field is extremely strong, the second field has little effect and the  $\Lambda$  system remains unexcited. This is because the resonance frequency of the  $\Lambda$  system is  $\omega_{31}$  when it occupies the ground level, and the second field is highly out of resonance.

However, the second field generates the dressed states by mixing  $|2\rangle$  and  $|3\rangle$ , and shifts the resonance of the  $\Lambda$  system. In figure 3(b), we plot the reflection coefficient  $|r(\mu_1)|$  of the first field as a function of  $\mu_1$  and  $|E_2|^2$ , fixing  $\mu_2 (= \omega_{32})$  and  $|E_1|^2 (= 10^5 \text{ s}^{-1})$ , (single-photon regime). We clearly observe the Rabi splitting of level  $|3\rangle$ . The dip frequencies can be fitted simply by  $\omega_{31} \pm \sqrt{\kappa_{32}}|E_2|$ , by considering the dressing between only two levels,  $|2\rangle$  and  $|3\rangle$ . However, this fitting breaks down when the second field is extremely strong, where level  $|1\rangle$  becomes involved in the formation of the dressed states [14]. In figure 3(c), we plot the reflection coefficient  $|r(\mu_1)|$  as a function of  $\mu_2$  and  $|E_2|^2$ , fixing  $\mu_1 (= \omega_{31})$  and  $|E_1|^2 (= 10^5 \text{ s}^{-1})$ , (single-photon regime). When the second field is absent or weak, reflection of the first field is prohibited nearly completely, as we discussed in section 3.1. However, as we increase  $|E_2|^2$ , the first field gradually goes out of resonance due to the Rabi splitting of level  $|3\rangle$  and the perfect extinction of the reflected wave breaks down. We observe a peak at  $\mu_2 = \omega_{32}$  ( $2\pi \times 9.94 \text{ MHz}$ ), which indicates the revival of reflection. The width of the revived peak is of the order of Rabi splitting induced by the second field,  $\sqrt{\kappa_{32}}|E_2|$ . The physical mechanism of this phenomenon is essentially the same as that of electromagnetically induced transparency (EIT) [11, 40]. The only difference is the following point: in EIT, the input field transmits the optical system when they do not interact. In contrast, in the present phenomenon, the input field is reflected at the end of the waveguide when the field does not interact with the  $\Lambda$  system. Another remarkable point in figure 3(b) is the asymmetric spectrum in the high-power region. This is due to excitation of the  $\omega_{31}$  transition ( $2\pi \times 10.02 \text{ GHz}$ ) by the second field.

The reflection coefficient of the second field,  $|r(\mu_2)|$ , is also plotted in figure 3(c). Since the levels  $|2\rangle$  and  $|3\rangle$  are nearly unoccupied (see figure 3(a)), the second field interacts with the  $\Lambda$  system only virtually. Therefore, the second field is almost unaffected in comparison with the

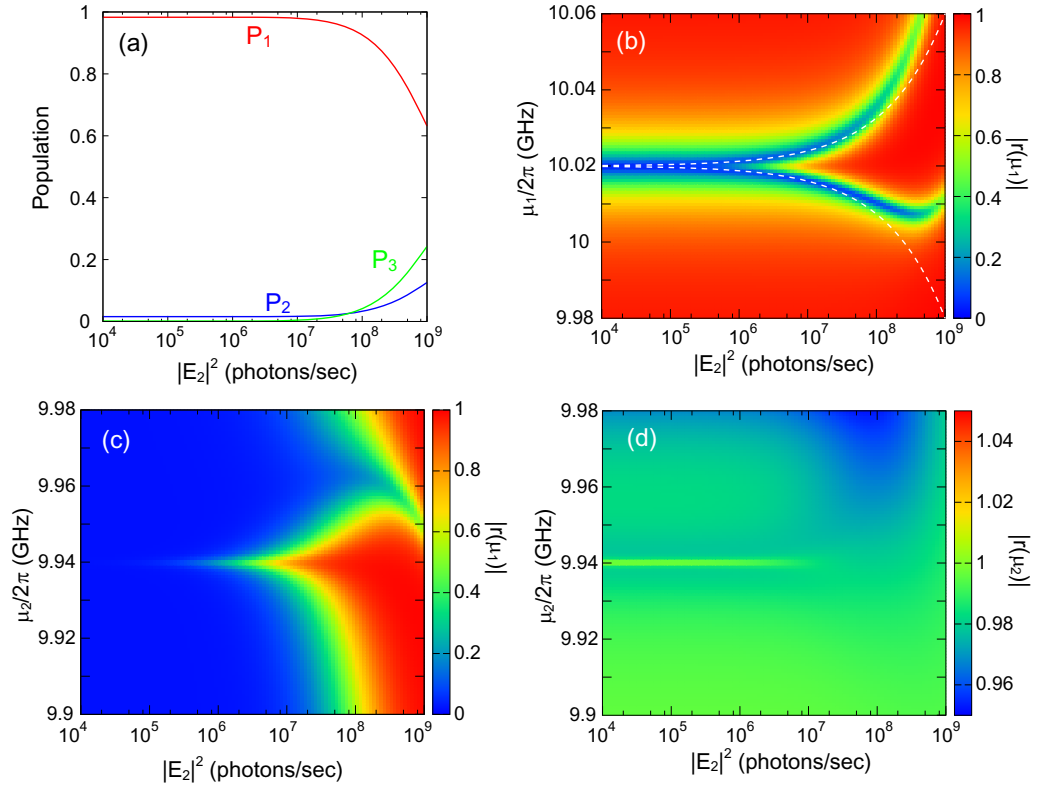


**Figure 3.** (a) Stationary populations of the three levels as functions of  $|E_2|^2$ . The other parameters are fixed at  $\mu_1 = \omega_{31}$ ,  $\mu_2 = \omega_{32}$  and  $|E_1|^2 = 10^{-5} \text{ s}^{-1}$  (single-photon regime). (b) Reflection coefficient  $|r(\mu_1)|$  of the first field as a function of  $\mu_1$  and  $|E_2|^2$ . The other parameters are  $\mu_2 = \omega_{32}$  and  $|E_1|^2 = 10^{-5} \text{ s}^{-1}$ . Rabi splitting of level  $|3\rangle$  induced by the second field is observed. The dip frequencies are fitted by  $\omega_{31} \pm \sqrt{\kappa_{32}}|E_2|$  (white dotted lines). (c) Reflection coefficient  $|r(\mu_1)|$  as a function of  $|E_2|^2$  and  $\mu_2$ . The other parameters are  $\mu_1 = \omega_{31}$  and  $|E_1|^2 = 10^{-5} \text{ s}^{-1}$ . The reflected wave revives by applying the second field. (d) Reflection coefficient  $|r(\mu_2)|$  of the second field as a function of  $\mu_2$  and  $|E_2|^2$ . The other parameters are  $\mu_1 = \omega_{31}$  and  $|E_1|^2 = 10^{-5} \text{ s}^{-1}$ .

first field. The background spectrum is asymmetric in the high-power region of figure 3(c) due to the  $\omega_{31}$  resonance.

### 3.3. Power spectrum

In this subsection, we discuss the power spectrum of the reflected field. We investigate the cases of a monochromatic input of the first field ( $\mu_1 \simeq \omega_{31}$ ) only. The second field ( $\mu_2 \simeq \omega_{32}$ ) does not yield remarkable effects on the power spectrum. The power spectrum is composed of the coherent part  $S_c(\omega)$  and the incoherent part  $S_i(\omega)$ , as we discussed in section 2.5. We mainly discuss the incoherent part here, since most of the input photons are scattered inelastically upon interaction with the impedance-matched  $\Lambda$  system.

We plot  $S_i(\omega)$  in figure 4(a), by fixing the input frequency at  $\mu_1 = \omega_{31}$  and varying the power  $|E_1|^2$ . In the single-photon regime ( $|E_1|^2 \lesssim \gamma_{21}$ ), we observe a dominant peak at the

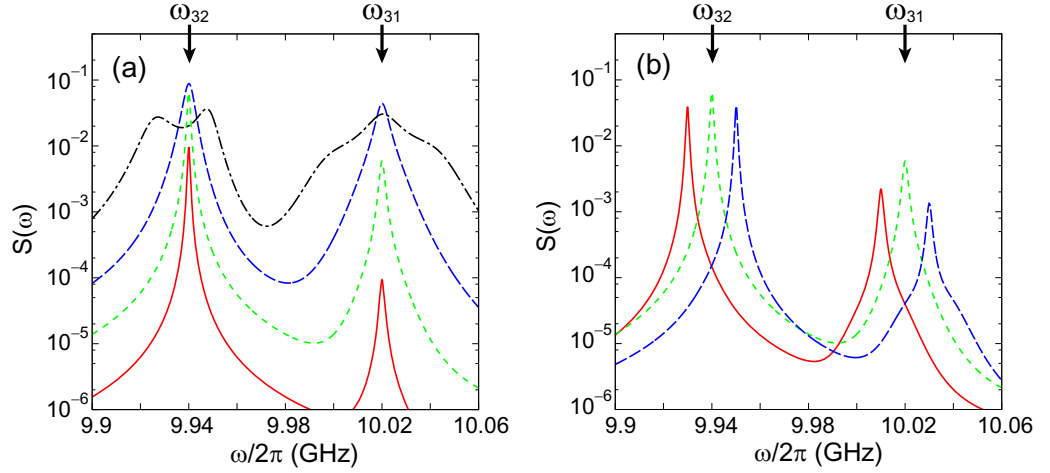


**Figure 4.** Spectral shapes of  $S_i(\omega)$ . (a) The input frequency is fixed at  $\mu_1 = \omega_{31}$  and the power is varied:  $|E_1|^2 = 10^5$  (solid),  $10^6$  (dotted),  $10^7$  (dashed) and  $10^8$  (dash-dotted). The down-converted peak ( $\omega_{32}$ ) is dominant in the single-photon regime ( $|E_1|^2 \lesssim \gamma_{21}$ ), implying the nearly deterministic down-conversion of the input photons. For a stronger input power ( $|E_1|^2 \gtrsim \gamma_{21}$ ), the conversion efficiency decreases. (b) The input power is fixed at  $|E_1|^2 = 10^6$  (single-photon regime) and the frequency is varied:  $\mu_1 = 10.01$  GHz (solid),  $10.02$  GHz (dotted) and  $10.03$  GHz (dashed). The down-converted peak is centered at  $\mu_1 - \omega_{21}$ .

down-converted frequency  $\omega_{32}$  and a much weaker peak at the input frequency  $\omega_{31}$ . Furthermore, as observed in figure 2(b), elastic scattering is strongly suppressed. Thus, most input photons are down-converted upon a single interaction with the  $\Lambda$  system. The spectral width is determined by  $\gamma_{21}$ , i.e. the inversed lifetime of level  $|2\rangle$ . The peak height increases linearly with the input power. In contrast, in the multi-photon regime ( $|E_1|^2 \gtrsim \gamma_{21}$ ), the spectrum becomes broader as the input power increases (power broadening) [41, 42]. We also observe that the peak at the input frequency becomes comparable to the peak at the down-converted frequency. Namely, the down-conversion efficiency decreases by increasing the input power. We plot  $S_i(\omega)$  in figure 4(b), by fixing the input power at  $|E_1|^2 = 10^5 \text{ s}^{-1}$  (single-photon regime) and varying the frequency  $\mu_1$ . As we increase the detuning  $|\mu_1 - \omega_{31}|$ , the interaction between the input field and the  $\Lambda$  system becomes weaker and the probability of inelastic scattering decreases. However, the spectral shape is almost unchanged. The down-converted peak appears at  $\mu_1 - \omega_{21}$ . Namely, the red-shift from the input frequency is always  $\omega_{21}$  ( $= 2\pi \times 80$  MHz).

We examine the properties of the down-converted photons in more detail. We define the down-conversion efficiency with the area of the down-converted peak normalized by the input flux, i.e.  $\int_{\omega'}^{\omega''} \frac{d\omega}{2\pi} S_i(\omega) / |E_1|^2$ , where we have chosen  $(\omega', \omega'')/2\pi = (9.9, 9.98)$  GHz. Figures 5(a) and (b) plot the conversion efficiency and the linewidth of the peak as functions of the input power, by assuming a resonant input ( $\mu_1 = \omega_{31}$ ). In order to observe the effects of the maximal down-conversion rate,  $\gamma_{21}$  is varied in figure 5. In the single-photon regime ( $|E_1|^2 \lesssim \gamma_{21}$ ), the  $\Lambda$  system responds to the input field linearly. The linewidth takes a constant value of  $\gamma_{21}/2\pi$  regardless of the input power. The down-conversion efficiency is analytically given by  $\kappa_{32}/(\kappa_{32} + \gamma_{31} + \gamma_{32})$  in the single-photon regime. Since  $\kappa_{32} \gg \gamma_{31}, \gamma_{32}$  in this system, the

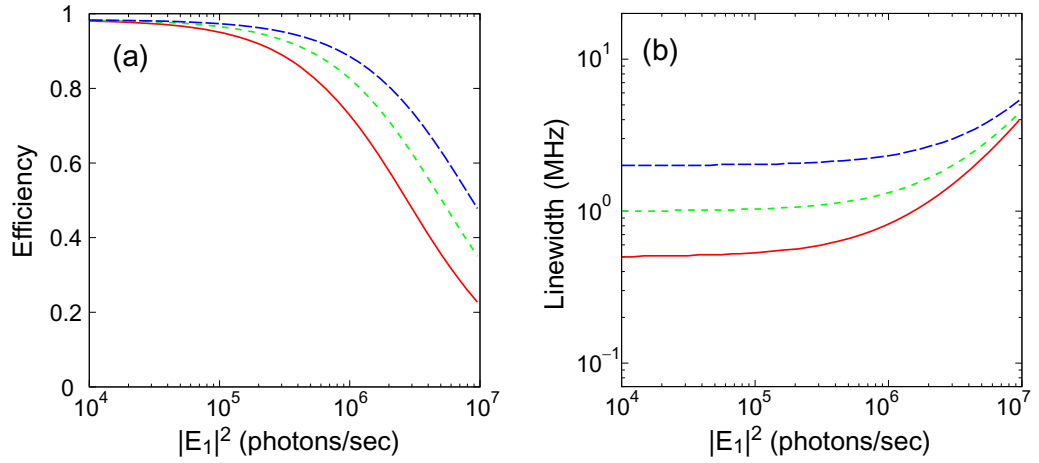


**Figure 5.** (a) Down-conversion efficiency and (b) linewidth of the down-converted peak, as functions of the input power  $|E_1|^2$ . The input frequency is fixed at  $\mu_1 = \omega_{31}$ .  $\gamma_{21}/2\pi = 0.5$  MHz (solid), 1 MHz (dotted) and 2 MHz (dashed). A larger  $\gamma_{21}$  avoids saturation (population of  $|2\rangle$ ) and therefore improves the down-conversion efficiency. The width of the down-converted peak is determined by  $\gamma_{21}$  for a weak input.

down-conversion efficiency is almost unity. In contrast, in the multi-photon regime ( $|E_1|^2 \gtrsim \gamma_{21}$ ), we observe nonlinear effects. The conversion efficiency decreases monotonically due to saturation, and the efficiency is halved when  $|E_1|^2 \simeq \gamma_{21}$ . We also confirm the power broadening of the spectral width [41, 42].

#### 4. Summary

We theoretically investigated the interaction between an impedance-matched  $\Lambda$  system and a semi-infinite waveguide field. By assuming a classical continuous field as the input, we analyzed the coherent amplitude and the power spectrum of the output (reflected) field. By the ratio of the maximal rate of the down-conversion and the input flux, we can define the single-photon and multi-photon regimes of the input power. In the single-photon regime, all of the input photons are down-converted deterministically. The coherent amplitude vanishes in the reflected field and the power spectrum has a dominant peak at the down-converted frequency. In the multi-photon regime, due to the saturation of the  $\Lambda$  system, we observe nonlinear optical effects such as power broadening in the spectrum and the decrease of the down-conversion efficiency. We also investigated the two-tone spectroscopy, showing that the additional field breaks the impedance matching and revives the coherent amplitude in the reflected field.

#### Acknowledgments

This work was supported in part by the Funding Program for World-Leading Innovative R&D on Science and Technology (FIRST), KAKENHI (25400417), SCOPE (111507004), NICT Commissioned Research, Project for Developing Innovation Systems of MEXT and the Research Foundation for Opto-Science and Technology.

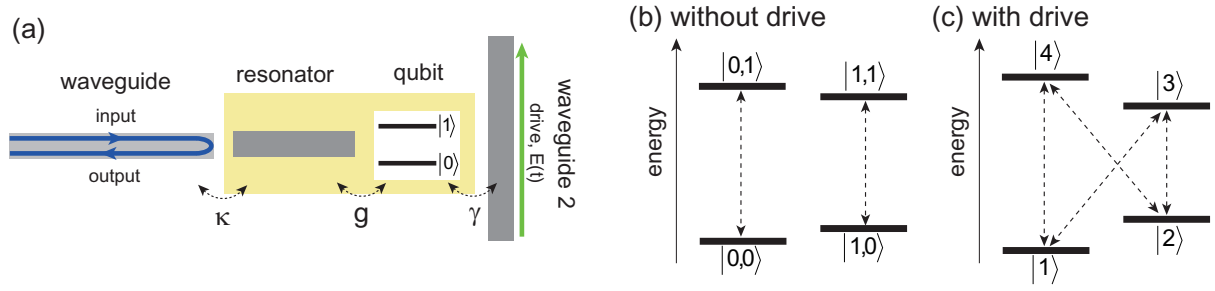


**Figure A.1.** (a) Schematic representation of the considered qubit–resonator system. (b) Energy diagram of the qubit–resonator system without driving ( $E = 0$ ).  $|m, n\rangle = |m\rangle_q |n\rangle_r$ . The diagram becomes nested for a properly chosen drive frequency ( $\omega_q - 3\chi < \omega_d < \omega_q - \chi$ ). (c) Energy diagram of the dressed states ( $E \neq 0$ ). Dotted lines in (b) and (c) indicate the allowed optical transitions. Oblique decay paths are generated by driving.

## Appendix A. Implementation in circuit quantum electrodynamics

Here, we outline how to implement an impedance-matched  $\Lambda$  system in circuit QED [35]. Figure A.1(a) is the schematic of the considered system [36]. It is composed of a driven qubit, a resonator and two waveguides. Waveguide 1 is the probe input/output port and waveguide 2 is the qubit drive port. This system is described by a driven Jaynes–Cummings Hamiltonian

$$\mathcal{H}(t) = \mathcal{H}_s(t) + \mathcal{H}_{sw} + \mathcal{H}_{se}, \quad (\text{A.1})$$

$$\mathcal{H}_s(t) = \omega_q \sigma^\dagger \sigma + \omega_r a^\dagger a + g(\sigma^\dagger a + a^\dagger \sigma) + \sqrt{\gamma}[E(t)\sigma^\dagger + E^*(t)\sigma], \quad (\text{A.2})$$

$$\mathcal{H}_{sw} = \int dk \left[ kb_k^\dagger b_k + \sqrt{\kappa/2\pi}(a^\dagger b_k + b_k^\dagger a) \right], \quad (\text{A.3})$$

$$\mathcal{H}_{se} = \int dk \left[ kc_k^\dagger c_k + \sqrt{\gamma/2\pi}(\sigma^\dagger c_k + c_k^\dagger \sigma) \right]. \quad (\text{A.4})$$

where  $\sigma$  and  $a$  are the annihilation operators for the qubit and the resonator, and  $b_k$  and  $c_k$  are the field operators for waveguides 1 and 2, respectively. The meanings of the parameters are as follows:  $\omega_q$  (qubit frequency),  $\omega_r$  (resonator frequency),  $g$  (qubit–resonator coupling),  $\kappa$  (decay rate of resonator into waveguide 1) and  $\gamma$  (decay rate of qubit into waveguide 2). The qubit drive is monochromatic,  $E(t) = Ee^{-i\omega_d t}$ . The parameter values are as follows:  $(\omega_q, \omega_r)/2\pi = (5, 10)$  GHz and  $(g, \kappa, \gamma)/2\pi = (500, 20, 1)$  MHz. Note that the qubit and the resonator are highly detuned and are coupled dispersively.

The Hamiltonian becomes static in the frame rotating at  $\omega_d$ . Then,  $\mathcal{H}_s = (\omega_q - \omega_d)\sigma^\dagger \sigma + (\omega_r - \omega_d)a^\dagger a + g(\sigma^\dagger a + a^\dagger \sigma) + \sqrt{\gamma}(E\sigma^\dagger + E^*\sigma)$ .  $\mathcal{H}_{sw}$  and  $\mathcal{H}_{se}$  remain unchanged except that the origin of frequency is shifted by  $\omega_d$ . We denote the product state of the qubit and the resonator by  $|i, j\rangle (= |i\rangle_q |j\rangle_r)$ , where  $i = 0, 1$  and  $j = 0, 1, \dots$ . When the drive is off ( $E = 0$ ), their eigenfrequencies are given, within the second-order perturbation in  $g$ , by  $\omega_{|0,n\rangle} = n(\omega_r - \omega_d + \chi)$  and  $\omega_{|1,n\rangle} = \omega_q - \omega_d - \chi + n(\omega_r - \omega_d - \chi)$ , where  $\chi = g^2/(\omega_r - \omega_q)$  is the dispersive level shift. Here, only the four lowest levels ( $|0, 0\rangle$ ,  $|0, 1\rangle$ ,  $|1, 0\rangle$  and  $|1, 1\rangle$ ) are relevant. In order to achieve the impedance matching by driving, it is necessary to make the energy diagram

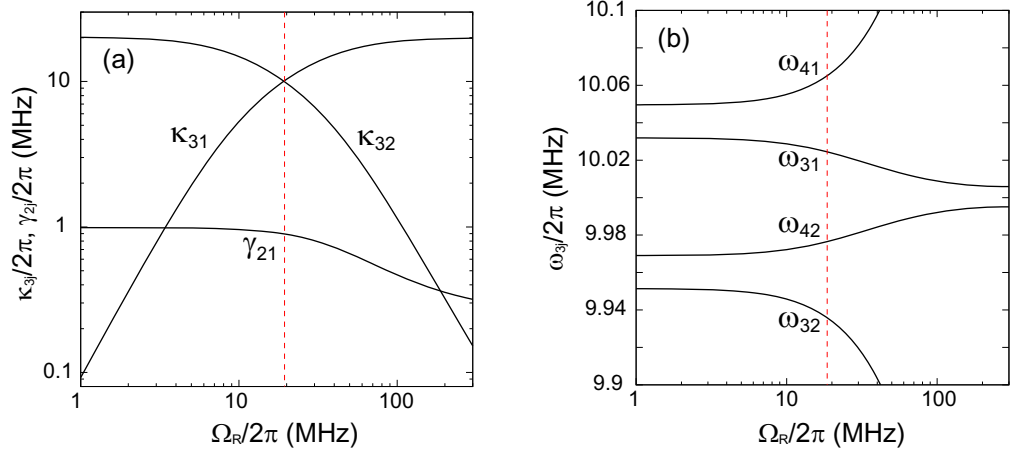


**Figure A.2.** (a) Decay rates ( $\kappa_{31}$ ,  $\kappa_{32}$  and  $\gamma_{21}$ ) and (b) transition frequencies ( $\omega_{31}$ ,  $\omega_{32}$ ,  $\omega_{41}$  and  $\omega_{42}$ , where  $\omega_{ij} = \omega_j - \omega_i$ ) as functions of the drive power. The impedance-matching condition is satisfied at  $\Omega_R/2\pi = 19$  MHz (dotted vertical line). At this point, the two lower states are almost unmixed, i.e.  $|1\rangle = |0\rangle_q|0\rangle_r$  and  $|2\rangle = |1\rangle_q|0\rangle_r$ .

nested as in figure A.1(b) [35]. Therefore, the drive frequency should be chosen to satisfy  $\omega_q - 3\chi < \omega_d < \omega_q - \chi$ . We set  $\omega_d/2\pi = 4.87$  GHz to satisfy this.

We refer to the eigenstates of  $\mathcal{H}_s$  as the dressed states and denote them and their frequencies by  $|n\rangle$  and  $\omega_n$  ( $n = 1, 2, \dots$ ). By switching to the dressed-state base, we obtain the static Hamiltonian of equation (1). The decay rates  $\kappa_{mn}$  and  $\gamma_{mn}$  of equation (1) are given by

$$\kappa_{mn} = \kappa |\langle m|a^\dagger|n\rangle|^2, \quad (\text{A.5})$$

$$\gamma_{mn} = \gamma |\langle m|\sigma^\dagger|n\rangle|^2. \quad (\text{A.6})$$

The drive field mixes the lower (higher) two levels in figure A.1(b) to form the dressed states  $|1\rangle$  and  $|2\rangle$  ( $|3\rangle$  and  $|4\rangle$ ) in figure A.1(c). We may use the three states  $|1\rangle$ ,  $|2\rangle$  and  $|3\rangle$  or  $|1\rangle$ ,  $|2\rangle$  and  $|4\rangle$  as the  $\Lambda$  system. We choose the former in the following. The decay is of resonator origin for  $|3\rangle \rightarrow |1\rangle$  and  $|3\rangle \rightarrow |2\rangle$ , whereas the decay is of qubit origin for  $|2\rangle \rightarrow |1\rangle$ . Figures A.2(a) and (b), respectively, plot the decay rates ( $\kappa_{31}$ ,  $\kappa_{32}$  and  $\gamma_{21}$ ) and the transition frequencies ( $\omega_{31}$ ,  $\omega_{32}$ ,  $\omega_{41}$  and  $\omega_{42}$  where  $\omega_{ij} = \omega_i - \omega_j$ ) as functions of the drive power. We employ the Rabi frequency of the qubit,  $\Omega_R = \sqrt{\gamma}|E|$ , as a measure of the drive power here. It is observed that the impedance-matching condition,  $\kappa_{31} = \kappa_{32}$ , can be satisfied at a drive power of  $\Omega_R/2\pi = 19$  MHz. At this drive power, the decay rates are  $(\kappa_{31}, \kappa_{32}, \gamma_{21})/2\pi \simeq (10, 10, 1)$  MHz and the transition frequencies are  $(\omega_{31}, \omega_{32})/2\pi \simeq (10.02, 9.94)$  GHz. Note that the drive frequency  $\omega_d$ , which has been subtracted in this section due to the rotating frame, is recovered here.

## Appendix B. Calculation of $S_i(\omega)$

Here we discuss technical details in the evaluation of  $S_i(\omega)$ . The two-point correlation functions,  $\langle \sigma_{uv}(t), \sigma_{ij}(t + \tau) \rangle$ , have the following properties: (i) the correlation between the two operators is lost in the  $\tau \rightarrow \infty$  limit. Therefore,  $\lim_{\tau \rightarrow \infty} \langle \sigma_{uv}(t), \sigma_{ij}(t + \tau) \rangle = 0$ . (ii) the equations of motion

for the two-point functions with respect to  $\tau (> 0)$  are the same as those for the one-point functions.

For calculation of  $S_i(\omega)$ , we introduce the following two quantities:

$$H_{uv,ij}^{pq}(\omega) = \frac{1}{\pi} \int_0^\infty d\tau e^{i(\omega - p\mu_1 - q\mu_2)\tau} \langle \sigma_{uv}, \sigma_{ij}(\tau) \rangle^{p,q}, \quad (\text{B.1})$$

$$J_{uv,ij}^{pq}(\omega) = \frac{1}{\pi} \int_0^\infty d\tau e^{i(\omega - p\mu_1 - q\mu_2)\tau} \frac{d}{d\tau} \langle \sigma_{uv}, \sigma_{ij}(\tau) \rangle^{p,q}, \quad (\text{B.2})$$

where the variable  $t$  is omitted for simplicity. By partially integrating equation (B.2),  $J_{uv,ij}^{pq} = -\langle \sigma_{uv}, \sigma_{ij} \rangle^{p,q} / \pi - i(\omega - p\mu_1 - q\mu_2) H_{uv,ij}^{pq}$ . We can evaluate  $\langle \sigma_{uv}, \sigma_{ij} \rangle^{p,q}$  from the one-point quantities as  $\langle \sigma_{uv}, \sigma_{ij} \rangle^{p,q} = \delta_{vi} s_{uj}^{p,q} - \sum_{p',q'} s_{uv}^{p-p',q-q'} s_{ij}^{p',q'}$ . On the other hand, from the equation of motion, we have  $J_{uv,ij}^{pq} = \sum_{m,n} (\eta_{ijmn}^{(1)} H_{uv,mn}^{p,q} - iE_1 \eta_{ijmn}^{(2)} H_{uv,mn}^{p+1,q} - \dots)$ . From these two equations, we have

$$-\frac{1}{\pi} \langle \sigma_{uv}, \sigma_{ij} \rangle^{p,q} - i(\omega - p\mu_1 - q\mu_2) H_{uv,ij}^{pq} = \sum_{m,n} \left( \eta_{ijmn}^{(1)} H_{uv,mn}^{p,q} - iE_1 \eta_{ijmn}^{(2)} H_{uv,mn}^{p+1,q} - \dots \right). \quad (\text{B.3})$$

Note that the right-hand side of equation (B.3) is obtained by replacing  $s_{mn}^{p,q}$  with  $H_{uv,mn}^{p,q}$  in equation (12). Since  $\sum_m \sigma_{mm} (= \hat{1})$  commutes with any operator, we replace one of the diagonal components with the following equality:

$$\sum_m H_{uv,mm}^{p,q} = 0. \quad (\text{B.4})$$

By solving the above simultaneous equations numerically, we can determine  $H_{uv,ij}^{p,q}(\omega)$ . The incoherent component of the spectrum,  $S_i(\omega)$ , is given by

$$S_i(\omega) = \text{Re} \sum_{u,v,i,j} \sqrt{\kappa_{uv} \kappa_{ji}} H_{uv,ij}^{0,0}(\omega). \quad (\text{B.5})$$

The validity of the numerical results is checked by the sum rule of  $\int d\omega S_i(\omega) = \text{Re} \sum_{u,v,i,j} \sqrt{\kappa_{uv} \kappa_{ji}} \langle \sigma_{uv}, \sigma_{ji} \rangle^{0,0}$ .

## References

- [1] Zheng H, Gauthier D J and Baranger H U 2010 *Phys. Rev. A* **82** 063816
- [2] Turchette Q A, Hood C J, Lange W, Mabuchi H and Kimble H J 1995 *Phys. Rev. Lett.* **75** 4710
- [3] Reithmaier J P, Sęk G, Löffler A, Hofmann C, Kuhn S, Reitzenstein S, Keldysh L V, Kulakovskii V D, Reinecke T L and Forchel A 2004 *Nature* **432** 197
- [4] Yoshie T, Scherer A, Hendrickson J, Khitrova G, Gibbs H M, Rupper G, Ell C, Shchekin O B and Deppe D G 2004 *Nature* **432** 200
- [5] Fushman I, Englund D, Faraon A, Stoltz N, Petroff P and Vukovic J 2008 *Science* **320** 769
- [6] Aoki T, Parkins A S, Alton D J, Regal C A, Dayan B, Ostby E, Vahala K J and Kimble H J 2009 *Phys. Rev. Lett.* **102** 083601
- [7] Hoi I C, Wilson C M, Johansson G, Palomaki T, Stace T M, Fan B and Delsing P 2012 arXiv:1207.1203
- [8] Shen J T and Fan S 2005 *Phys. Rev. Lett.* **95** 213001
- [9] Astafiev O, Zagoskin A M, Abdumalikov A A Jr, Pashkin Y A, Yamamoto T, Inomata K, Nakamura Y and Tsai J S 2010 *Science* **327** 840

- [10] Hoi I C, Palomaki T, Lindkvist J, Johansson G, Delsing P and Wilson C M 2012 *Phys. Rev. Lett.* **108** 263601
- [11] Abdumalikov A A Jr, Astafiev O V, Zagoskin A M, Pashkin Y A, Nakamura Y and Tsai J S 2010 *Phys. Rev. Lett.* **104** 193601
- [12] Astafiev O V, Abdumalikov A A Jr, Zagoskin A M, Pashkin Y A, Nakamura Y and Tsai J S 2010 *Phys. Rev. Lett.* **104** 183603
- [13] Hoi I C, Wilson C M, Johansson G, Palomaki T, Peropadre B and Delsing P 2011 *Phys. Rev. Lett.* **107** 073601
- [14] Koshino K, Terai H, Inomata K, Yamamoto T, Qiu W, Wang Z and Nakamura Y 2013 *Phys. Rev. Lett.* **110** 263601
- [15] Bozyigit D *et al* 2011 *Nature Phys.* **7** 154
- [16] Eichler C, Lang C, Fink J M, Govenius J, Filipp S and Wallraff A 2012 *Phys. Rev. Lett.* **109** 240501
- [17] Lang C, Eichler C, Steffen L, Fink J M, Woolley M J, Blais A and Wallraff A 2013 *Nature Phys.* **9** 345
- [18] Yin Y *et al* 2013 *Phys. Rev. Lett.* **110** 107001
- [19] Vetsch E, Reitz D, Sague G, Schmidt R, Dawkins S T and Rauschenbeutel A 2010 *Phys. Rev. Lett.* **104** 203603
- [20] Huck A, Kumar S, Shakoov A and Andersen U L 2011 *Phys. Rev. Lett.* **106** 096801
- [21] Hwang J, Pototschnig M, Lettow R, Zumofen G, Renn A, Götzinger S and Sandoghdar V 2012 *Nature* **460** 76
- [22] Stobińska M, Alber G and Leuchs G 2012 *Europhys. Lett.* **86** 14007
- [23] Koshino K 2009 *Phys. Rev. A* **79** 013804
- [24] Koshino K, Ishizaka S and Nakamura Y 2010 *Phys. Rev. A* **82** 010301
- [25] Gea-Banacloche J and Pedrotti L M 2011 *Phys. Rev. A* **83** 042333
- [26] Gea-Banacloche J and Pedrotti L M 2012 *Phys. Rev. A* **86** 052311
- [27] Chang D E, Sorensen A S, Demler E A and Lukin M D 2007 *Nature Phys.* **3** 807
- [28] Witthaut D and Sorensen A S 2010 *New J. Phys.* **12** 043052
- [29] Witthaut D, Lukin M D and Sorensen A S 2012 *Europhys. Lett.* **97** 50007
- [30] Ciccarello F, Browne D E, Kwek L C, Schomerus H, Zarcone M and Bose S 2012 *Phys. Rev. A* **85** 050305
- [31] Zheng H, Gauthier D J and Baranger H U 2013 *Phys. Rev. Lett.* **111** 090502
- [32] Romero G, Garcia-Ripoll J J and Solano E 2009 *Phys. Rev. Lett.* **102** 173602
- [33] Chen Y F, Hover D, Sendelbach S, Maurer L, Merkel S T, Pritchett E J, Wilhelm F K and McDermott R 2011 *Phys. Rev. Lett.* **107** 217401
- [34] Peropadre B, Romero G, Johansson G, Wilson C M, Solano E and Garcia-Ripoll J J 2011 *Phys. Rev. A* **84** 063834
- [35] Koshino K, Inomata K, Yamamoto T and Nakamura Y 2013 *Phys. Rev. Lett.* **111** 153601
- [36] Inomata K, Yamamoto T, Billangeon P M, Nakamura Y and Tsai J S 2012 *Phys. Rev. B* **86** 140508
- [37] Koshino K and Nakamura Y 2012 *New J. Phys.* **14** 043005
- [38] Gea-Banacloche J 2013 *Phys. Rev. A* **87** 023832
- [39] Walls D F and Milburn G J 1995 *Quantum Optics* (New York: Springer)
- [40] Harris S E 1997 *Phys. Today* **50** 36
- [41] Allen L and Eberly J H 1975 *Optical Resonance and Two Level Atoms* (New York: Dover)
- [42] Citron M L, Gray H R, Gabel C W and Stroud C R Jr 1977 *Phys. Rev. A* **16** 1507